Automotive Science and Engineering, Vol. 14, No. 1, (2024), 4327-4352

Iran University of Science and Technology

Automotive Science and Engineering

Journal Homepage: ase.iust.ac.ir

ISSN: 2008-9899

Improving Structural Failure of Bus Roof Panel Stiffened by Novel Multi-layered Semi-circular Corrugated Woven Carbon Fiber Reinforced Polymer (CFRP) plates

M. Shirzadifar [1*], ***J. Marzbanrad*** [2]

[1] PhD Graduated Student at School of Automotive Engineering, Iran University of Science and Technology, Tehran, Iran

[2] Faculty at School of Automotive Engineering, Iran University of Science and Technology, Tehran, Iran

ARTICLE INFO

Article history:

Received : 21 Jan 2024

Accepted: 20 Mar 2024

Published: 28 Mar 2024

Keywords:

CFRP Plates

Corrugated Woven Plates Dynamic Loading

Composite Plate Impact Failure

Bus Rollover

A B S T R A C T

The corrugated composite plates have wide application to improve the energy absorption and failure behavior of panel structures. The roof panel of the bus could benefit from the use of these structures to reduce impact failures in rollover accidents. The aim of this paper is to design a new configuration of bus roof panels stiffened with multi-layer semi-circular corrugated CFRP plates to minimize structure failure during rollover accidents. An analytical failure equation of Tsai-Hill index for the new proposed panel subjected to dynamic impact loading has been derived. The failure equation was validated using FEM methods and digital image correlation impact tests. According to the roll over impact situation, the multi-layered semi-circular corrugated woven CFRP roof panel displays a positive failure behavior of 89%.

1.Introduction

The wave structure of corrugated composite plates is designed to enhance structural panel stiffness and energy absorption. The Corrugated composite plates with potential application in aerospace, civil, and automotive industries are classified based on their wave shapes. In corrugated composite structures, wave features are designed to transmit bending and twisting loads, as well as shear between two separated surfaces. Since corrugated composite plates have a high stiffness due to their light weight, new types of them have been designed over the last decade. In 2010, G. Kress and M.Winkler developed a homogenization material model in order to describe the loads of flat corrugated multidirectional composite sheets [1]. For corrugated composite plates subjected to different types of bending and twisting forces, their analytical results provided all the information about stress, strain, and displacement distributions. Hyo Seon Ji and colleagues designed a GFRP corrugated superstructure bridge in 2010. In comparison with conventional bridges, corrugated FRP bridges have the same dynamic and static responses loaded by trucks, and they cost 25 percent less [2]. Analytical equation of stiffness properties for corrugated panels was suggested by Y. Xia and colleagues in 2012 [3]. Their equivalent model could be used for any corrugated shape panels. In 2012, Wernberg and

*Corresponding Author
Email Address: mohammad_shirzadifar@auto.iust.ac.ir
http://doi.org/10.22068/ase.2024.668

colleagues used FRP corrugated sheets incorporated into the body structure of a railway vehicle to reduce the car body's weight by half [4]. As well as replacing the conventional vehicle's body structure, the corrugated sandwich panels could meet mechanical requirements. The corrugated composite materials used inside the vehicle's crash box were examined by M. Costas et al in 2013 [5]. In their study, a combination of glass-fiber reinforced polyamide padding and a steel box with good crashworthiness parameters was recommended. Also M. Winkler and G. Kress approached a finite element program with planar elements to realize anisotropy of corrugated laminates in 2013 [6]. Natural Bamboo fiber was used in corrugated laminated composites by Zehui Jiang and colleagues in 2013 [7]. Their experimental study found that bamboo fiber corrugated shapes had positive effects on impact tests. C. Thurnherr and colleagues developed equations for calculating the center-point deflection of composite material corrugated panels subjected to pressure in 2016 [8]. Their

stated beam – equation modelling is valid for corrugated panels. Additionally, a higher-order beam model was used to investigate failure initiation in curved laminates in

2017 [9]. As the thickness of a corrugated laminate increases, the critical stress component shifts from intralaminar hoop stress to interlaminar shear stress. Hongyong Jiang and colleagues proposed a progressive damage model to research the effects of composite corrugated beam trigger geometry on their crashworthiness and damage behaviors in 2017 [10]. In order to reduce peak crashworthiness loads, they recommended a convex trigger with bevel trigger angles of 45-degrees and 60-degrees for corrugated beams. In 2017, Yiru Ren and colleagues improved another progressive damage model to predict crashworthy of composite corrugated plate [11]. They considered both of the intra- and inter- laminar failure behavior. Their improved stacked shell model indicated good agreement with the impact loading and interlaminar failure of the composite corrugated structure. They also proposed a novel aircraft energy absorption strut system equipped with a corrugated composite plate to improve crashworthiness in 2017 [12]. In 2018, Mou and colleagues studied the damage behavior and the energy-absorbing properties of the sinusoidal corrugated composite plate using a finite element model. [13]. manufacturing void defects have influence on energy absorption characteristics of flexural CFRP plates. Mehdikhani et al. reviewed considerable void defects influence on mechanical properties of CFRP plates in 2018 [14].

Rong Yu et al. investigated the effects of geometric configurations of sandwich panels equipped with arc, sinusoidal, rectangular, trapezoidal and triangular corrugated cores in 2018[15]. They introduced trapezoidal corrugated core as the ideal shape under planar compression tests. Z. Zhang and colleagues designed a new sandwich panel consisting of multi- layered modified sinusoidal corrugated core in 2019 [16]. A quasi-static compression test was conducted on the new proposed sandwich panel to determine its compressive modules and ultimate strength. Mohammadabadi et al. Suggested an analytical model to evaluate the bending behavior of a corrugated wood base panel in 2019 [17]. Their model considered the deformation of the corrugated core subjected to pure tension, compression and shear loads. The researchers found that replacing the corrugated core with a continuous layer improved the panels' crashworthiness. Ch. Affolter et.al tested the failure modes of a novel dimpled laminate plates to facilitate the access of rescue vehicles and equipment in soft and muddy ground in 2019 [18]. A. Farrokhabadi and colleagues designed a new type of multi- layered corrugated sandwich panels in 2020 [19]. Their experimental and numerical analysis of multi-layered corrugated plates indicated rectangular geometry of wave patterns have better results in terms of energy absorption and specific energy in comparison to trapezoidal and triangular wave shapes. In recent decade, different novel multi-layered corrugated sandwich panels were introduced and used as crushable sacrifice structures. Yinan Wang and Fu-Kuo Chang presented a novel multifunctional energy storage composites to decrease mechanical damage and failure modes of thin battery layers [20].

Almost all papers about them investigated their mechanical behavior under quasi static compression or 3 point bending tests [21]. Further, the effects of using them discussed without considering their mechanical behavior while directly subjected to dynamic crushing loading. However, despite extensive use of novel corrugated composite panels in different industries to improve mechanical failures [22-25], there is no evidence of their use in vehicle roof panels to decrease structure failures in rollover accidents.

This study investigated the mechanical behavior of multi-layered semi-circular corrugated bi-directional woven CFRP plates subjected to scale-down dynamic impact loadings during rollovers. We have developed an analytical failure equation for multi-layered semi-circular corrugated woven CFRP plates subjected to concentrated dynamic impact force. An analytical and numerical study is performed on samples with several dimensions of novel multi-layered semi-circular corrugated woven CFRP plates with different stacking sequences, wave feature ratios and plies thickness. To examin the failure of a heavy bus roof panel stiffened with corrugated semi-circular woven CFRP plates, a digital image correlation (DIC) method was employed in accordance with the FMVSS 220 rollover standard.

1. Multi-layered semi-circular corrugated woven carbon fiber reinforced polymer (CFRP) plates

The Multi-layer semi-circular corrugated woven CFRP plate unit consists of three semi-circular corrugated laminates having the same thickness and stacking sequence, but with different ratios of wave feature geometry as shown in Figure 1. Symmetric patterns are stacked and the layers are woven bi-directionally. Furthermore, each pattern lamina must have at least 2 layers to be symmetric. The outer pattern has the maximum radius and minimum wave number, but the inner pattern has the maximum wave number and minimum radius along the longitudinal of each unit. Inner and middle patterns have radius to wave number ratios of 1/16 and 1/4, respectively. Furthermore,

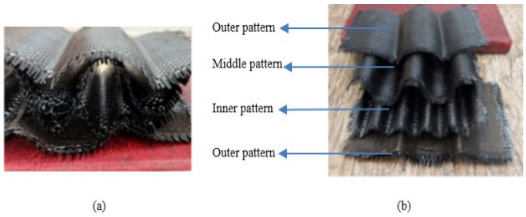

Figure 1: Schematic diagram of: (a) A multi-layered semi-circular corrugated woven CFRP plate unit; (b) The Outer, middle and inner patterns of multi-layer semi-circular corrugated woven CFRP plate unit

the outer pattern's radius depends on the maximum space available for placing each unit.

2. Methodology of evaluating multi-layered semi-circular corrugated woven CFRP unit

To capture the effect of each multi-layered semi-circular corrugated woven CFRP unit on firs layer failure when subjected to dynamic impact loadings from rollovers, an 8 ton bus roof panel was employed as shown in Figure2. The maximum available space for placing each unit could be considered 130.75mm according to maximum allowable plate displacements Based on FMVSS 220 rollover standard [26]. To make the analytical, numerical, and experimental results comparable, a scaling procedure for the impact parameters of the roof panel in Table 1 is applied based on the "Texas Barrel Barrier Test" [27].

3. Analytical methodology of evaluating multi-layered semi-circular corrugated woven CFRP unit

The first step to obtaining an analytical failure equation for the multi-layered semi-circular corrugated woven CFRP unit is determining the flat plate deflection under dynamic impact loading (F) on the composite flat plate. Each flat laminate's out-of-plane deflection, $w_{(k)}$, to the situation in Figure 3 is calculated by Equation (1) based on Reference [28].

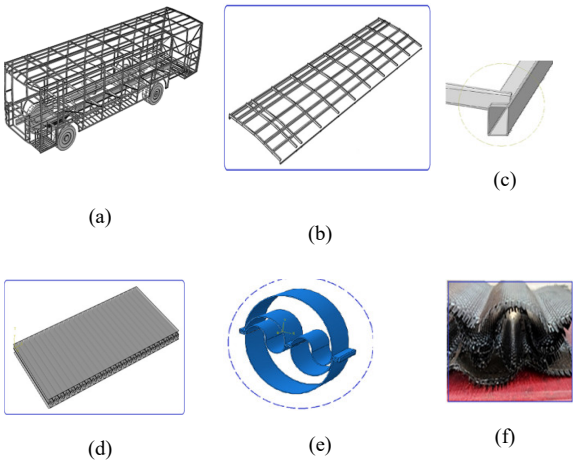

(a) (b) (c) (d) (e) (f)

Figure 2: An 8 ton bus roof panel equipped with multi- layered semi-circular corrugated woven CFRP plate: (a) Bus roof panel; (b) Conventional roof panel; (c) Rectangular cross section of conventional roof panel; (d) Roof panel equipped with multi-layer semi-circular corrugated woven CFRP unit; (e) Corrugated woven CFRP unit cross section; (f) Corrugated woven CFRP unit

Table 1: Scale down parameters of an 8 ton bus roof panel rollover

Actual Parameters	Actual amount	Scale down parameters	Scale down amount
Bus curb weight	7716.47 (kg)	Impactor weight	6.374 (kg)
Rollover impact	113.32 (kN)	Impactor force	62.53 (N)
Bus roof panel dimension	11990.4×914.4 (mm^2)	Scale down sample dimension	125×75 (mm^2)
Rollover impact velocity	15.6 ($\frac{m}{sec}$)	Impactor velocity	4.48 ($\frac{m}{sec}$)
Rollover impact energy	172.71 (kJ)	Impactor energy	64(J)
		Impactor drop height	1.023 (m)
Scale down factor = 12.192			

As the plate's boundary is symmetrical, there is no bending-twisting coupling and out of plane deflection. $D_{16} = D_{26} = 0$, around the plate's perimeter . Out of plan stress is also neglected. The applied dynamic impact loading expressed with the use of delta function (m and n are Fourier series counter).

$$w_{(k)} = \sum_{m=1}^{\infty}\sum_{n=1}^{\infty} \frac{\frac{4F}{ab}\sin\left(\frac{m\ \pi x_0}{a}\right)\sin\left(\frac{n\pi y_0}{b}\right)\sin\left(\frac{m\ \pi x}{a}\right)\sin\left(\frac{n\pi y}{b}\right)}{D_{(k),11}\left(\frac{m\ \pi}{a}\right)^4 + 2\left(D_{(k),12} + 2D_{(k),66}\right)\frac{m^2 n^2 \pi^4}{a^2 b^2} + D_{(k),22}\left(\frac{n\ \pi}{b}\right)^4} \quad (1)$$

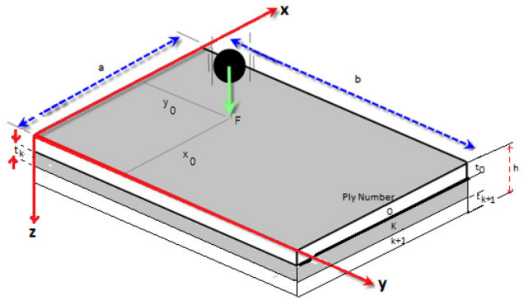

Figure 3: Composite flat plate subjected to dynamic impact loading

$D_{(k),11}$, $D_{(k),12}$, $D_{(k),22}$ and $D_{(k),66}$ are bending stiffness for each flat laminate. The bending stiffness can be calculated from the longitudinal and transverse Young's modulus (E_L, E_T), Poisson's ratios (υ_{LT}, υ_{TL}), shear modulus (G_{LT}) and standard transformation tensor ($Q^{\theta_k}_{(k),ij}$) based on ply rotated angle (θ_k) according to Equations (2), (3) and (4).

$$\begin{aligned} Q_{(k),xx} &= \frac{E_L}{1-\upsilon_{LT}\upsilon_{TL}} \\ Q_{(k),yy} &= \frac{E_T}{1-\upsilon_{LT}\upsilon_{TL}} \\ Q_{(k),xy} &= \frac{\upsilon_{LT}E_T}{1-\upsilon_{LT}\upsilon_{TL}} \\ Q_{(k),ss} &= G_{LT} \end{aligned} \tag{2}$$

and

$$\begin{aligned} Q^{\theta_k}_{(k),11} &= cos^4(\theta_k)Q_{(k),xx} + sin^4(\theta_k)Q_{(k),yy} + 2cos^2(\theta_k)sin^2(\theta_k)Q_{(k),xy} \\ &\quad + 4cos^2(\theta_k)sin^2(\theta_k)Q_{(k),ss} \\ Q^{\theta_k}_{(k),22} &= sin^4(\theta_k)Q_{(k),xx} + cos^4(\theta_k)Q_{(k),yy} + 2cos^2(\theta_k)sin^2(\theta_k)Q_{(k),xy} \\ &\quad + 4cos^2(\theta_k)sin^2(\theta_k)Q_{(k),ss} \\ Q^{\theta_k}_{(k),12} &= cos^2(\theta_k)sin^2(\theta_k)\big(Q_{(k),xx} + Q_{(k),yy}\big) + \big(cos^4(\theta_k) + sin^4(\theta_k)\big)Q_{(k),xy} \\ &\quad - 4cos^2(\theta_k)sin^2(\theta_k)Q_{(k),ss} \\ Q^{\theta_k}_{(k),66} &= cos^2(\theta_k)sin^2(\theta_k)\big(Q_{(k),xx} + Q_{(k),yy}\big) - 2cos^2(\theta_k)sin^2(\theta_k)Q_{(k),xy} \\ &\quad + (cos^2(\theta_k) - sin^2(\theta_k))^2Q_{(k),ss} \\ Q^{\theta_k}_{(k),16} &= cos^3(\theta_k)\,sin(\theta_k)Q_{(k),xx} \\ &\quad - sin^3(\theta_k)\,cos(\theta_k)Q_{(k),yy} \\ &\quad + (cos(\theta_k)sin^3(\theta_k) - cos^3(\theta_k)\,sin(\theta_k))(Q_{(k),xy} + 2Q_{(k),ss}) \\ Q^{\theta_k}_{(k),26} &= sin^3(\theta_k)\,cos(\theta_k)Q_{(k),xx} \\ &\quad - cos^3(\theta_k)\,sin(\theta_k)Q_{(k),yy} \\ &\quad + (sin(\theta_k)sin^3(\theta_k) - sin^3(\theta_k)\,cos(\theta_k))(Q_{(k),xy} + 2Q_{(k),ss}) \end{aligned} \tag{3}$$

and

$$\begin{cases} D_{(k),ij} = \dfrac{1}{3}\displaystyle\sum_{k=1}^{N} Q^{\theta_k}_{(k),ij}\left(z^3_k - z^3_{k-1}\right) \\ N = Layer\ \ number,\quad i,j = 1,2,6 \end{cases} \tag{4}$$

In the following sections, the equations of plane strains and stresses are derived from the out-of-plane deflection of each flat laminate, $w_{(k)}$, subjected to dynamic impact loading respectively as Equations (5) and (6) [29]. Also Tsai-Hill failure can be calculated from Equation (7) according to Equations (8), (9) and (10).

$$\begin{cases} \varepsilon_x^k(x,y) = z_k \sum_{m=1}^{\infty}\sum_{n=1}^{\infty} \dfrac{\dfrac{4F}{ab}\sin\left(\dfrac{m\pi x_0}{a}\right)\sin\left(\dfrac{n\pi y_0}{b}\right)\left(\dfrac{m^2\pi^2}{a^2}\right)\sin\left(\dfrac{m\pi x}{a}\right)\sin\left(\dfrac{n\pi y}{b}\right)}{D_{(k),11}\left(\dfrac{m\ \pi}{a}\right)^4 + 2\left(D_{(k),12}+2D_{(k),66}\right)\dfrac{m^2n^2\pi^4}{a^2b^2} + D_{(k),22}\left(\dfrac{n\ \pi}{b}\right)^4} \\ \varepsilon_y^k(x,y) = z_k \sum_{m=1}^{\infty}\sum_{n=1}^{\infty} \dfrac{\dfrac{4F}{ab}\sin\left(\dfrac{m\pi x_0}{a}\right)\sin\left(\dfrac{n\pi y_0}{b}\right)\left(\dfrac{n^2\pi^2}{b^2}\right)\sin\left(\dfrac{m\pi x}{a}\right)\sin\left(\dfrac{n\pi y}{b}\right)}{D_{(k),11}\left(\dfrac{m\ \pi}{a}\right)^4 + 2\left(D_{(k),12}+2D_{(k),66}\right)\dfrac{m^2n^2\pi^4}{a^2b^2} + D_{(k),22}\left(\dfrac{n\ \pi}{b}\right)^4} \\ \varepsilon_{xy}^k(x,y) = z_k \sum_{m=1}^{\infty}\sum_{n=1}^{\infty} \left(\dfrac{\dfrac{4F}{ab}\sin\left(\dfrac{m\pi x_0}{a}\right)\sin\left(\dfrac{n\pi y_0}{b}\right)}{D_{(k),11}\left(\dfrac{m\ \pi}{a}\right)^4 + 2\left(D_{(k),12}+2D_{(k),66}\right)\dfrac{m^2n^2\pi^4}{a^2b^2} + D_{(k),22}\left(\dfrac{n\ \pi}{b}\right)^4} \right)^2 \left(\dfrac{mn\pi^2}{ab}\right)\sin\left(\dfrac{2m\pi x}{a}\right)\sin\left(\dfrac{2n\pi y}{b}\right) \end{cases} \tag{5}$$

$$\begin{bmatrix} \sigma_x^k \\ \sigma_y^k \\ \tau_{xy}^k \end{bmatrix} =$$

$$\begin{bmatrix} \boldsymbol{Q}_{(k),11}^{\boldsymbol{\theta}_k} & \boldsymbol{Q}_{(k),12}^{\boldsymbol{\theta}_k} & \boldsymbol{Q}_{(k),16}^{\boldsymbol{\theta}_k} \\ \boldsymbol{Q}_{(k),12}^{\boldsymbol{\theta}_k} & \boldsymbol{Q}_{(k),22}^{\boldsymbol{\theta}_k} & \boldsymbol{Q}_{(k),26}^{\boldsymbol{\theta}_k} \\ \boldsymbol{Q}_{(k),16}^{\boldsymbol{\theta}_k} & \boldsymbol{Q}_{(k),26}^{\boldsymbol{\theta}_k} & \boldsymbol{Q}_{(k),66}^{\boldsymbol{\theta}_k} \end{bmatrix}$$

$$\begin{bmatrix} \boldsymbol{z_k}\displaystyle\sum_{\boldsymbol{m=1}}^{\infty}\sum_{\boldsymbol{n=1}}^{\infty} \dfrac{\boldsymbol{\frac{4F}{ab}\sin\left(\frac{m\pi x_0}{a}\right)\sin\left(\frac{n\pi y_0}{b}\right)\left(\frac{m^2\pi^2}{a^2}\right)\sin\left(\frac{m\pi x}{a}\right)\sin\left(\frac{n\pi y}{b}\right)}}{\boldsymbol{D_{(k),11}\left(\frac{m\pi}{a}\right)^4 + 2\frac{m^2n^2\pi^4}{a^2b^2}\left(D_{(k),12}+2D_{(k),66}\right) + D_{(k),22}\left(\frac{n\pi}{b}\right)^4}} \\ \boldsymbol{z_k}\displaystyle\sum_{\boldsymbol{m=1}}^{\infty}\sum_{\boldsymbol{n=1}}^{\infty} \dfrac{\boldsymbol{\frac{4F}{ab}\sin\left(\frac{m\pi x_0}{a}\right)\sin\left(\frac{n\pi y_0}{b}\right)\left(\frac{n^2\pi^2}{b^2}\right)\sin\left(\frac{m\pi x}{a}\right)\sin\left(\frac{n\pi y}{b}\right)}}{\boldsymbol{D_{(k),11}\left(\frac{m\pi}{a}\right)^4 + 2\frac{m^2n^2\pi^4}{a^2b^2}\left(D_{(k),12}+2D_{(k),66}\right) + D_{(k),22}\left(\frac{n\pi}{b}\right)^4}} \\ \boldsymbol{z_k}\displaystyle\sum_{\boldsymbol{m=1}}^{\infty}\sum_{\boldsymbol{n=1}}^{\infty} \left(\dfrac{\boldsymbol{\frac{4F}{ab}\sin\left(\frac{m\pi x_0}{a}\right)\sin\left(\frac{n\pi y_0}{b}\right)}}{\boldsymbol{D_{(k),11}\left(\frac{m\pi}{a}\right)^4 + 2\frac{m^2n^2\pi^4}{a^2b^2}\left(D_{(k),12}+2D_{(k),66}\right) + D_{(k),22}\left(\frac{n\pi}{b}\right)^4}} \right)^2 \left(\boldsymbol{\frac{mn\pi^2}{ab}\sin\left(\frac{2m\pi x}{a}\right)\sin\left(\frac{2n\pi y}{b}\right)}\right) \end{bmatrix} \tag{6}$$

$$T^{(k)} = \frac{\left(\sigma_1^k\right)^2}{X^2} + \frac{\left(\sigma_2^k\right)^2}{Y^2} - \sigma_1^k\sigma_2^k\left(\frac{1}{X^2}+\frac{1}{Y^2}\right) + \frac{\left(\tau_{12}^k\right)^2}{S_{12}} \tag{7}$$

That is,

$$\sigma_1^k = Z_k \sum_{m=1}^{\infty}\sum_{n=1}^{\infty}\left(\frac{\frac{4F\pi^2}{ab}sin\left(\frac{m\pi x_0}{a}\right)sin\left(\frac{n\pi y_0}{b}\right)}{D_{(k),11}\left(\frac{m\pi}{a}\right)^4+2\left(\frac{m^2n^2\pi^4}{a^2b^2}\right)\left(D_{(k),12}+2D_{(k),66}\right)+D_{(k),22}\left(\frac{n\pi}{b}\right)^4}\right.$$
$$\left(\left(\left(\frac{Q^{\theta(k)}_{(k),11}m^2}{a^2}+\frac{Q^{\theta(k)}_{(k),12}n^2}{b^2}\right)sin\left(\frac{m\pi x}{a}\right)sin\left(\frac{n\pi y}{b}\right)\right)+\right.$$
$$\left.\left.\left(\sum_{m=1}^{\infty}\sum_{n=1}^{\infty}\left(\frac{\frac{4F}{ab}sin\left(\frac{m\pi x_0}{a}\right)sin\left(\frac{n\pi y_0}{b}\right)}{D_{(k),11}\left(\frac{m\pi}{a}\right)^4+2\left(\frac{m^2n^2\pi^4}{a^2b^2}\right)\left(D_{(k),12}+2D_{(k),66}\right)+D_{(k),22}\left(\frac{n\pi}{b}\right)^4}\right)\right.\right.$$
$$\left.\left.\left(\frac{mnQ^{\theta(k)}_{(k),16}}{ab}sin\left(\frac{2m\pi x}{a}\right)sin\left(\frac{2n\pi y}{b}\right)\right)\right)\right) \quad (8)$$

and

$$\sigma_2^k = Z_k \sum_{m=1}^{\infty}\sum_{n=1}^{\infty}\left(\frac{\frac{4F\pi^2}{ab}sin\left(\frac{m\pi x_0}{a}\right)sin\left(\frac{n\pi y_0}{b}\right)}{D_{(k),11}\left(\frac{m\pi}{a}\right)^4+2\left(\frac{m^2n^2\pi^4}{a^2b^2}\right)\left(D_{(k),12}+2D_{(k),66}\right)+D_{(k),22}\left(\frac{n\pi}{b}\right)^4}\right.$$
$$\left(\left(\left(\frac{Q^{\theta(k)}_{(k),12}m^2}{a^2}+\frac{Q^{\theta(k)}_{(k),22}n^2}{b^2}\right)sin\left(\frac{m\pi x}{a}\right)sin\left(\frac{n\pi y}{b}\right)\right)+\right.$$
$$\left.\left.\left(\sum_{m=1}^{\infty}\sum_{n=1}^{\infty}\left(\frac{\frac{4F}{ab}sin\left(\frac{m\pi x_0}{a}\right)sin\left(\frac{n\pi y_0}{b}\right)}{D_{(k),11}\left(\frac{m\pi}{a}\right)^4+2\left(\frac{m^2n^2\pi^4}{a^2b^2}\right)\left(D_{(k),12}+2D_{(k),66}\right)+D_{(k),22}\left(\frac{n\pi}{b}\right)^4}\right)\right.\right.$$
$$\left.\left.\left(\frac{mnQ^{\theta(k)}_{(k),26}}{ab}sin\left(\frac{2m\pi x}{a}\right)sin\left(\frac{2n\pi y}{b}\right)\right)\right)\right) \quad (9)$$

and

$$\tau_{12}^{k}=Z_k\sum_{m=1}^{\infty}\sum_{n=1}^{\infty}\left(\frac{\frac{4F\pi^2}{ab}sin\left(\frac{m\pi x_0}{a}\right)sin\left(\frac{n\pi y_0}{b}\right)}{D_{(k),11}\left(\frac{m\pi}{a}\right)^4+2\left(\frac{m^2n^2\pi^4}{a^2b^2}\right)\left(D_{(k),12}+2D_{(k),66}\right)+D_{(k),22}\left(\frac{n\pi}{b}\right)^4}\right)$$
$$\left(\left(\left(\frac{Q_{(k),16}^{\theta(k)}m^2}{a^2}+\frac{Q_{(k),26}^{\theta(k)}n^2}{b^2}\right)sin\left(\frac{m\pi x}{a}\right)sin\left(\frac{n\pi y}{b}\right)\right)+\left(\sum_{m=1}^{\infty}\sum_{n=1}^{\infty}\left(\frac{\frac{4F}{ab}sin\left(\frac{m\pi x_0}{a}\right)sin\left(\frac{n\pi y_0}{b}\right)}{D_{(k),11}\left(\frac{m\pi}{a}\right)^4+2\left(\frac{m^2n^2\pi^4}{a^2b^2}\right)\left(D_{(k),12}+2D_{(k),66}\right)+D_{(k),22}\left(\frac{n\pi}{b}\right)^4}\right)\left(\frac{mnQ_{(k),66}^{\theta(k)}}{ab}sin\left(\frac{2m\pi x}{a}\right)sin\left(\frac{2n\pi y}{b}\right)\right)\right)\right) \quad (10)$$

In order to modify the composite flat plate strain, stress and Tsai-Hill failure equations for multi- layered semi- circular corrugated woven CFRP plate unit, instead of flat plate stiffness, $\left[D_{(k),ij}\right]$, curved beam stiffness, $\left[D'_{(k),ij}\right]$ must be used. It can be considered based on Figure 4 and Equation (11) [30].

$$\left[D'_{(k),ij}\right]=\begin{bmatrix}D'_{(k),11} & D'_{(k),12} & D'_{(k),16}\\ D'_{(k),21} & D'_{(k),22} & D'_{(k),26}\\ D'_{(k),16} & D'_{(k),26} & D'_{(k),66}\end{bmatrix}=\left[R\sum_{k=1}^{N}Q_{(k),ij}^{q_k}\left[\frac{1}{2}\left(z_k^2-z_{k-1}^2\right)-R\left(z_k-z_{k-1}\right)+R^2ln\left(\frac{R+z_k}{R+z_{k-1}}\right)\right]\right]_{i,j=1,2,6} \quad (11)$$

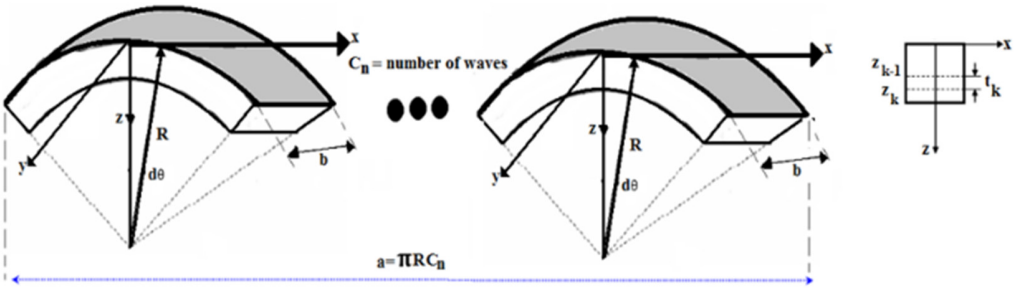

Figure 4: Curved beam geometry for calculating bending stiffness

Also the longitudinal of semi- circular corrugated woven plate, a, can be calculated from Equation (12) according to wave radius, R, and wave numbers, C_n.

$$a=\pi RC_n \tag{12}$$

Thus analytical out of plane deflection for multi-layered semi-circular woven plate, $w'_{(k)}$, is obtained in Equation 13 by substituting Equations (2), (3), (11) and (12) in Equation (1).

$$w'_{(k)}=\sum_{m=1}^{\infty}\sum_{n=1}^{\infty}\frac{\frac{4F}{b\pi R\,C_n}sin\left(\frac{m\;x_0}{R\;C_n}\right)sin\left(\frac{npy_0}{b}\right)sin\left(\frac{m\;x}{R\;C_n}\right)sin\left(\frac{npy}{b}\right)}{D'_{(k),11}\left(\frac{m}{R\;C_n}\right)^4+2\left(D'_{(k),12}+2D'_{(k),66}\right)\frac{m^2n^2p^2}{R^2C_n^2b^2}+D'_{(k),22}\left(\frac{n\;p}{b}\right)^4} \tag{13}$$

As in previous for flat composite plate, propagations of strains, stresses and failure of multi- layered semi-circular woven plate unit are obtained respectively in Equations (14), (15) and (16) according to out of plane deflection, $w'_{(k)}$, and classical laminated- plate theory (Equations 17, 18 and 19).

$$\begin{cases}
\varepsilon'^{\,k}_{x}(x,y)=z_k\sum_{m=1}^{\infty}\sum_{n=1}^{\infty}\dfrac{\frac{4F}{b\pi RC_n}sin\left(\frac{mx_0}{RC_n}\right)sin\left(\frac{n\pi y_0}{b}\right)\left(\frac{m^2}{R^2C_n^2}\right)sin\left(\frac{mx}{RC_n}\right)sin\left(\frac{n\pi y}{b}\right)}{D'_{(k),11}\left(\frac{m}{R\;C_n}\right)^4+2\left(D'_{(k),12}+2D'_{(k),66}\right)\frac{m^2n^2\pi^2}{R^2C_n^2b^2}+D'_{(k),22}\left(\frac{n\;\pi}{b}\right)^4} \\
\varepsilon'^{\,k}_{y}(x,y)=z_k\sum_{m=1}^{\infty}\sum_{n=1}^{\infty}\dfrac{\frac{4F}{b\pi RC_n}sin\left(\frac{mx_0}{RC_n}\right)sin\left(\frac{n\pi y_0}{b}\right)\left(\frac{n^2\pi^2}{b^2}\right)sin\left(\frac{mx}{RC_n}\right)sin\left(\frac{n\pi y}{b}\right)}{D'_{(k),11}\left(\frac{m}{R\;C_n}\right)^4+2\left(D'_{(k),12}+2D'_{(k),66}\right)\frac{m^2n^2\pi^2}{R^2C_n^2b^2}+D'_{(k),22}\left(\frac{n\;\pi}{b}\right)^4} \\
\varepsilon'^{\,k}_{xy}(x,y)=z_k\sum_{m=1}^{\infty}\sum_{n=1}^{\infty}\left(\dfrac{\frac{4F}{b\pi RC_n}sin\left(\frac{mx_0}{RC_n}\right)sin\left(\frac{n\pi y_0}{b}\right)}{D'_{(k),11}\left(\frac{m}{R\;C_n}\right)^4+2\left(D'_{(k),12}+2D'_{(k),66}\right)\frac{m^2n^2\pi^2}{R^2C_n^2b^2}+D'_{(k),22}\left(\frac{n\;\pi}{b}\right)^4}\right)^2 \\
\left(\frac{mn\pi}{bRC_n}\right)sin\left(\frac{2mx}{RC_n}\right)sin\left(\frac{2n\pi y}{b}\right)
\end{cases} \tag{14}$$

$$\begin{bmatrix}\acute{\sigma}_x^k\\ \acute{\sigma}_y^k\\ \acute{\tau}_{xy}^k\end{bmatrix} = \tag{15}$$

$$\begin{bmatrix}Q_{(k),11}^{\theta_k} & Q_{(k),12}^{\theta_k} & Q_{(k),16}^{\theta_k}\\ Q_{(k),12}^{\theta_k} & Q_{(k),22}^{\theta_k} & Q_{(k),26}^{\theta_k}\\ Q_{(k),16}^{\theta_k} & Q_{(k),26}^{\theta_k} & Q_{(k),66}^{\theta_k}\end{bmatrix}\begin{bmatrix} z_k\sum_{m=1}^{\infty}\sum_{n=1}^{\infty}\frac{\frac{4F}{b\pi RC_n}\sin\left(\frac{mx_0}{RC_n}\right)\sin\left(\frac{n\pi y_0}{b}\right)\left(\frac{m^2}{R^2C_n^2}\right)\sin\left(\frac{mx}{RC_n}\right)\sin\left(\frac{n\pi y}{b}\right)}{\acute{D}_{(k),11}\left(\frac{m}{RC_n}\right)^4+2\frac{m^2n^2\pi^2}{R^2C_n^2b^2}\left(\acute{D}_{(k),12}+2\acute{D}_{(k),66}\right)+\acute{D}_{(k),22}\left(\frac{n\pi}{b}\right)^4}\\ z_k\sum_{m=1}^{\infty}\sum_{n=1}^{\infty}\frac{\frac{4F}{b\pi RC_n}\sin\left(\frac{mx_0}{RC_n}\right)\sin\left(\frac{n\pi y_0}{b}\right)\left(\frac{n^2\pi^2}{b^2}\right)\sin\left(\frac{mx}{RC_n}\right)\sin\left(\frac{n\pi y}{b}\right)}{\acute{D}_{(k),11}\left(\frac{m}{RC_n}\right)^4+2\frac{m^2n^2\pi^2}{R^2C_n^2b^2}\left(\acute{D}_{(k),12}+2\acute{D}_{(k),66}\right)+\acute{D}_{(k),22}\left(\frac{n\pi}{b}\right)^4}\\ z_k\sum_{m=1}^{\infty}\sum_{n=1}^{\infty}\left(\frac{\frac{4F}{b\pi RC_n}\sin\left(\frac{mx_0}{RC_n}\right)\sin\left(\frac{n\pi y_0}{b}\right)}{\acute{D}_{(k),11}\left(\frac{m}{RC_n}\right)^4+2\frac{m^2n^2\pi^2}{R^2C_n^2b^2}\left(\acute{D}_{(k),12}+2\acute{D}_{(k),66}\right)+\acute{D}_{(k),22}\left(\frac{n\pi}{b}\right)^4}\right)^2\left(\frac{mn\pi\pi}{bRC_n}\sin\left(\frac{2mx}{RC_n}\right)\sin\left(\frac{2n\pi y}{b}\right)\right)\end{bmatrix}$$

$$T'^{(k)} = \frac{\left(\sigma_1'^k\right)^2}{X^2}+\frac{\left(\sigma_2'^k\right)^2}{Y^2}-\sigma_1'^k\sigma_2'^k\left(\frac{1}{X^2}+\frac{1}{Y^2}\right)+\frac{\left(\tau_{12}'^k\right)^2}{S_{12}} \tag{16}$$

That is,

$$\sigma_1'^k = Z_k\sum_{m=1}^{\infty}\sum_{n=1}^{\infty}\left(\frac{\frac{4F}{b\pi RC_n}sin\left(\frac{mx_0}{RC_n}\right)sin\left(\frac{n\pi y_0}{b}\right)}{D'_{(k),11}\left(\frac{m}{RC_n}\right)^4+2\left(\frac{m^2n^2\pi^2}{b^2R^2C^2{}_n}\right)\left(D'_{(k),12}+2D'_{(k),66}\right)+D'_{(k),22}\left(\frac{n\pi}{b}\right)^4}\right)\left(\left(\left(\frac{Q^{\theta(k)}_{(k),11}m^2}{R^2C^2{}_n}+\frac{Q^{\theta(k)}_{(k),12}n^2\pi^2}{b^2}\right)sin\left(\frac{mx}{RC_n}\right)sin\left(\frac{n\pi y}{b}\right)\right)+\left(\left(\sum_{m=1}^{\infty}\sum_{n=1}^{\infty}\left(\frac{\frac{4F}{b\pi RC_n}sin\left(\frac{mx_0}{RC_n}\right)sin\left(\frac{n\pi y_0}{b}\right)}{D'_{(k),11}\left(\frac{m}{RC_n}\right)^4+2\left(\frac{m^2n^2\pi^2}{b^2R^2C^2{}_n}\right)\left(D'_{(k),12}+2D'_{(k),66}\right)+D'_{(k),22}\left(\frac{n\pi}{b}\right)^4}\right)\times\left(\frac{mn\pi Q^{\theta(k)}_{(k),16}}{bRC_n}sin\left(\frac{2mx}{RC_n}\right)sin\left(\frac{2n\pi y}{b}\right)\right)\right)\right)\right) \tag{17}$$

and

$$\sigma'^{k}_{2} = Z_k \sum_{m=1}^{\infty}\sum_{n=1}^{\infty}\left(\frac{\frac{4F}{b\pi R C_n}\sin\left(\frac{m x_0}{R C_n}\right)\sin\left(\frac{n\pi y_0}{b}\right)}{D'_{(k),11}\left(\frac{m}{R C_n}\right)^4 + 2\left(\frac{m^2 n^2 \pi^2}{b^2 R^2 C^2_n}\right)\left(D'_{(k),12} + 2D'_{(k),66}\right) + D'_{(k),22}\left(\frac{n\pi}{b}\right)^4}\right)$$
$$\left(\left(\left(\frac{Q^{\theta(k)}_{(k),12} m^2}{R^2 C^2_n} + \frac{Q^{\theta(k)}_{(k),22} n^2\pi^2}{b^2}\right)\sin\left(\frac{m x}{R C_n}\right)\sin\left(\frac{n\pi y}{b}\right)\right) + \left(\sum_{m=1}^{\infty}\sum_{n=1}^{\infty}\left(\frac{\frac{4F}{b\pi R C_n}\sin\left(\frac{m x_0}{R C_n}\right)\sin\left(\frac{n\pi y_0}{b}\right)}{D'_{(k),11}\left(\frac{m}{R C_n}\right)^4 + 2\left(\frac{m^2 n^2 \pi^2}{b^2 R^2 C^2_n}\right)\left(D'_{(k),12} + 2D'_{(k),66}\right) + D'_{(k),22}\left(\frac{n\pi}{b}\right)^4}\right)\times \left(\frac{m n \pi Q^{\theta(k)}_{(k),26}}{b R C_n}\sin\left(\frac{2 m x}{R C_n}\right)\sin\left(\frac{2 n\pi y}{b}\right)\right)\right)\right) \quad (18)$$

and

$$\tau'^{k}_{12} = Z_k \sum_{m=1}^{\infty}\sum_{n=1}^{\infty}\left(\frac{\frac{4F}{b\pi R C_n}\sin\left(\frac{m x_0}{R C_n}\right)\sin\left(\frac{n\pi y_0}{b}\right)}{D'_{(k),11}\left(\frac{m}{R C_n}\right)^4 + 2\left(\frac{m^2 n^2 \pi^2}{b^2 R^2 C^2_n}\right)\left(D'_{(k),12} + 2D'_{(k),66}\right) + D'_{(k),22}\left(\frac{n\pi}{b}\right)^4}\right)$$
$$\left(\left(\left(\frac{Q^{\theta(k)}_{(k),16} m^2}{R^2 C^2_n} + \frac{Q^{\theta(k)}_{(k),26} n^2\pi^2}{b^2}\right)\sin\left(\frac{m x}{R C_n}\right)\sin\left(\frac{n\pi y}{b}\right)\right) + \left(\sum_{m=1}^{\infty}\sum_{n=1}^{\infty}\left(\frac{\frac{4F}{b\pi R C_n}\sin\left(\frac{m x_0}{R C_n}\right)\sin\left(\frac{n\pi y_0}{b}\right)}{D'_{(k),11}\left(\frac{m}{R C_n}\right)^4 + 2\left(\frac{m^2 n^2 \pi^2}{b^2 R^2 C^2_n}\right)\left(D'_{(k),12} + 2D'_{(k),66}\right) + D'_{(k),22}\left(\frac{n\pi}{b}\right)^4}\right)\times \left(\frac{m n \pi Q^{\theta(k)}_{(k),66}}{b R C_n}\sin\left(\frac{2 m x}{R C_n}\right)\sin\left(\frac{2 n\pi y}{b}\right)\right)\right)\right) \quad (19)$$

In Table 2, material properties of woven CFRP laminate used in this study were found out from hand lay-up coupons (Figure (5)) made up of 200 $\frac{gr}{m^2}$ woven carbon fibre and ML506 Epoxy resin with 47% volume fraction based on ASTMD3039M standards [31].

By substitutig the parameters of Table 1 and 2 into Equations (14), (15) and (16), the plane strain, stress and Tsai-Hill failure of multi-layered semi-circular corrugated woven CFRP plates subjected to dynamic impact loading can be calculated. Maximum of above parameters were plotted in Figures 6 to 8 for different wave ratios and plies thickness with $[0^{\circ}\text{-}90^{\circ}]$ and $[+45^{\circ},-45^{\circ}]$ stacking sequences in comparison with same parameters category of flat plate. The wave ratios $(\frac{2R}{C_N})$ for outer, middle and inner patterns of multi- layered semi-circular corrugated woven CFRP plate unit and also flat plate were considered respectively, 1.25, 5, 125 and 0 mm.

The minimum Tsai-Hill failure index occurred in the outer pattern of the multi-layered semi-circular corrugated woven CFRP plate unit subjected to an impact loading as shown in Figures 6 to 8. In Figure 9, the effect of different stacking sequences was investigated to determine the angle of the fibers which would produce the minimum failure index of the outer pattern. According to Figure 10, different stacking sequences have different effects on the decrease percent of Tsai-Hill index of the outer pattern in comparison with flat plates while being subjected to an impact load.

4. Numerical methodology of evaluating Multi-layered corrugated woven CFRP plate unit

Based on Figures 6 to10, the minimum Tsai-Hill failure index for outer, middle and inner patterns was achieved for two woven layers with stacking sequences of [0°-90°] and [+45°,-45°] under dynamic impact loading. Figures 11 to 18 show the comparison between the numerical analysis of outer, middle and inner patterns and the flat plates with stacking sequences of [0°-90°] and [+45°,-45°]. Mesh settings after mesh study, boundary and load conditions are also indicated for each pattern in Figures 11 to 18. Presented results in Figures 11 to 18 in terms of strain, stress, and failure index of multi-layered semi-circular corrugated woven CFRP plate units are good evidence that the derived equations are reliable when comparing multi-layered corrugated CFRP plate units and composite flat plates.

ABAQUS implicit solver was used for FEM simulations of multi-layered corrugated woven CFRP plates subjected to latitudinal impact. The geometry and material specifications of each multi-layered corrugated woven plate were defined according to Tables 1 and 2. The applied impact was also defined along the transverse direction according to the depicted boundary conditions in Figures 11 to 18(v1= v3= vR1= vR2= vR3=0). Each CFRP plate constrained around the clamps with U1=U2=U3=UR1= UR2=UR3=0. The FEM's recommended default parameters, rigid R3D4 and C3D8 hexahedral elements were employed to improve the analyses convergence. According to the performed mesh study for the reported strain results, the mentioned above mesh setup was reliable for the FEM studies.

Figure 5: Standard samples to find material behaviors of the woven CFRP laminate

Table 2: Material behaviors of woven CFRP laminate

$200\ \frac{gr}{m^2}$ woven CFRP laminate cured by ML506 epoxy resin with 47% volume fraction	MPa						
	X_t	X_c	Y_t	Y_c	Z_t	Z_c	S_{12}
Layer thickness of each woven laminate=0.3mm	399.7	239.8	399.7	239.8	80	80	40
	GPa						
	E_{11}	E_{22}	E_{33}	G_{12}	G_{13}	G_{23}	
Density ($\frac{kg}{m^3}$)	45.12	40.9	3.59	3.374	1.21	1.21	
	ϑ_{12}		ϑ_{13}		ϑ_{23}		
1666	0.074		0.4		0.4		

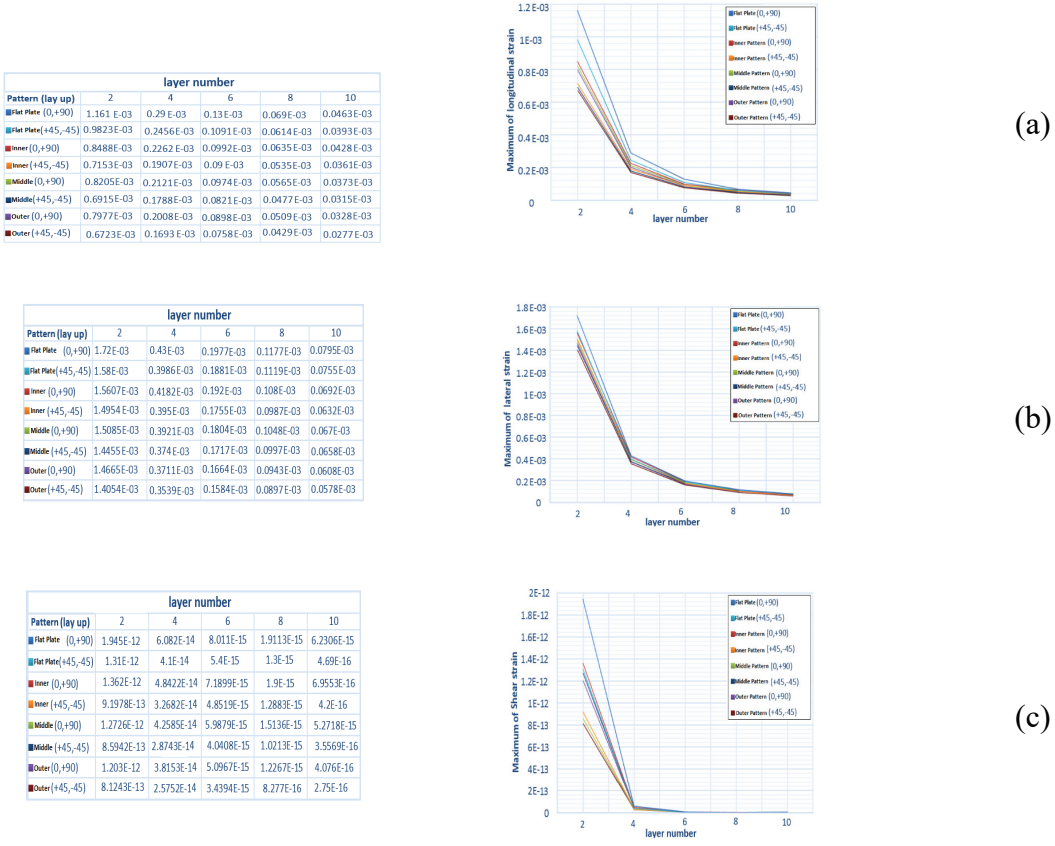

Figure 6: Outer, middle and inner patterns maximum plane strain of multi- layered semi-circular corrugated woven CFRP plate unit subjected to dynamic impact loading for different plies thickness with [0°-90°] and[+45°,-45°] stacking sequences in comparison with same parameters category of flat plate: (a) Longitudinal strain; (b) Lateral strain; (c) Shear strain

Pattern (lay up)	layer number 2	4	6	8	10
Flat Plate (0,+90)	86.564	21.7	9.6351	5.42	3.47
Flat Plate(+45,-45)	85.86	21.465	9.54	5.4	3.43
Inner (0,+90)	68.1	18.1874	8.6	5.112	3.45
Inner (+45,-45)	72.0051	19.1953	9.0581	5.39	3.425
Middle (0,+90)	65.816	17.0555	7.8373	4.5512	3.0035
Middle (+45,-45)	66.096	18.0013	8.2664	4.8	3.1662
Outer (0,+90)	63.989	16.1432	7.2304	4.097	2.641
Outer (+45,-45)	67.673	17.039	7.6265	4.3201	2.7841

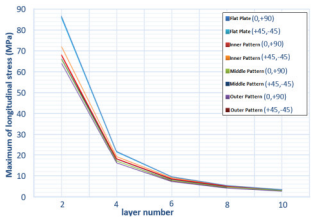

(a)

Pattern (lay up)	layer number 2	4	6	8	10
Flat Plate (0,+90)	113.53	28.5	12.7	7.13	4.565
Flat Plate(+45,-45)	90.18	22.545	10.02	5.64	3.61
Inner (0,+90)	98.24	26.306	12.4322	7.0403	4.49975
Inner (+45,-45)	77.745	20.7254	9.7802	5.48	3.527
Middle (0,+90)	65.816	24.6677	11.345	6.6	4.3505
Middle (+45,-45)	75.151	19.4362	8.9254	5.1814	3.4186
Outer (0,+90)	92.3126	23.3473	10.466	5.9328	3.8252
Outer (+45,-45)	73.0675	18.3973	8.2345	4.6644	3.006

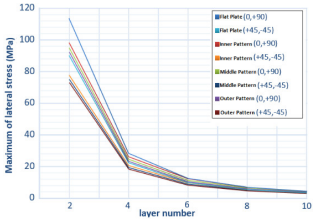

(b)

Pattern (lay up)	layer number 2	4	6	8	10
Flat Plate (0,+90)	6.48E-09	2.052E-10	2.7E-11	6.442E-12	2.3254E-12
Flat Plate(+45,-45)	3.13	0.7821	0.35	0.1992	0.1344
Inner (0,+90)	4.6E-09	1.634E-10	2.426E-11	6.415E-12	2.07E-12
Inner (+45,-45)	2.661	0.71	0.335	0.1955	0.1251
Middle (0,+90)	4.3E-09	1.44E-10	2.023E-11	5.107E-12	1.7787E-12
Middle (+45,-45)	2.5723	0.6653	0.3055	0.1773	0.117
Outer (0,+90)	4.06E-09	1.29E-10	1.72E-11	4.14E-12	1.3752E-12
Outer (+45,-45)	2.5009	0.6297	0.2818	0.1597	0.1029

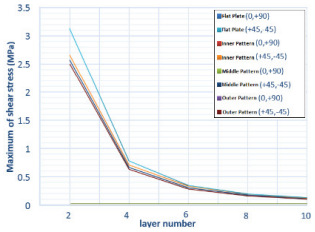

(c)

Figure 7: Outer, middle and inner patterns maximum plane stress of multi- layered semi-circular corrugated woven CFRP plate unit subjected to dynamic impact loading for different plies thickness with [0°-90°] and [+45°,-45°] stacking sequences in comparison with same parameters category of flat plate: (a) Longitudinal strain; (b) Lateral strain; (c) Shear strain

Pattern (lay up)	layer number 2	4	6	8	10
Flat Plate (0,+90)	1.5401	0.0967	0.0191	0.0061	0.0026
Flat Plate(+45,-45)	1.4546	0.0909	0.018	0.0059	0.0028
Inner (0,+90)	1.0257	0.0734	0.0164	0.0058	0.0025
Inner (+45,-45)	1.0519	0.0748	0.0166	0.0057	0.0023
Middle (0,+90)	0.9583	0.0646	0.0136	0.0046	0.002
Middle (+45,-45)	0.9829	0.0657	0.0139	0.0047	0.002
Outer (0,+90)	0.9058	0.0578	0.0116	0.0037	0.0016
Outer (+45,-45)	0.9292	0.0589	0.0118	0.0038	0.0016

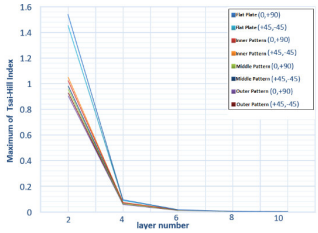

Figure 8: Outer, middle and inner patterns maximum Tsai-Hill failure index of semi-circular corrugated unit subjected to dynamic impact loading with stacking sequences of [0°-90°] and [+45°,-45°] in comparison with flat plate

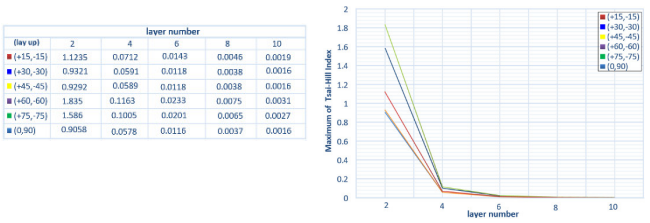

layer number					
(lay up)	2	4	6	8	10
(+15,-15)	1.1235	0.0712	0.0143	0.0046	0.0019
(+30,-30)	0.9321	0.0591	0.0118	0.0038	0.0016
(+45,-45)	0.9292	0.0589	0.0118	0.0038	0.0016
(+60,-60)	1.835	0.1163	0.0233	0.0075	0.0031
(+75,-75)	1.586	0.1005	0.0201	0.0065	0.0027
(0,90)	0.9058	0.0578	0.0116	0.0037	0.0016

Figure 9: Outer pattern maximum Tsai-Hill failure index of multi- layered semi-circular corrugated woven CFRP plate unit with different plies thickness and stacking sequences while subjected to dynamic impact loadings

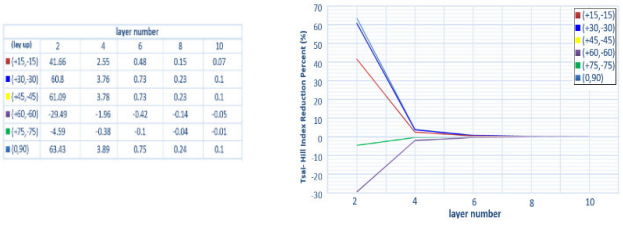

layer number					
(lay up)	2	4	6	8	10
(+15,-15)	41.66	2.55	0.48	0.15	0.07
(+30,-30)	60.8	3.76	0.73	0.23	0.1
(+45,-45)	61.09	3.78	0.73	0.23	0.1
(+60,-60)	-29.49	-1.96	-0.42	-0.14	-0.05
(+75,-75)	4.59	-0.38	-0.1	-0.04	-0.01
(0,90)	63.43	3.89	0.75	0.24	0.1

Figure 10: Effects of different stacking sequences on the decrease percent of Tsai-Hill index of the outer pattern in comparison with flat plate while subjected to dynamic impact loadings

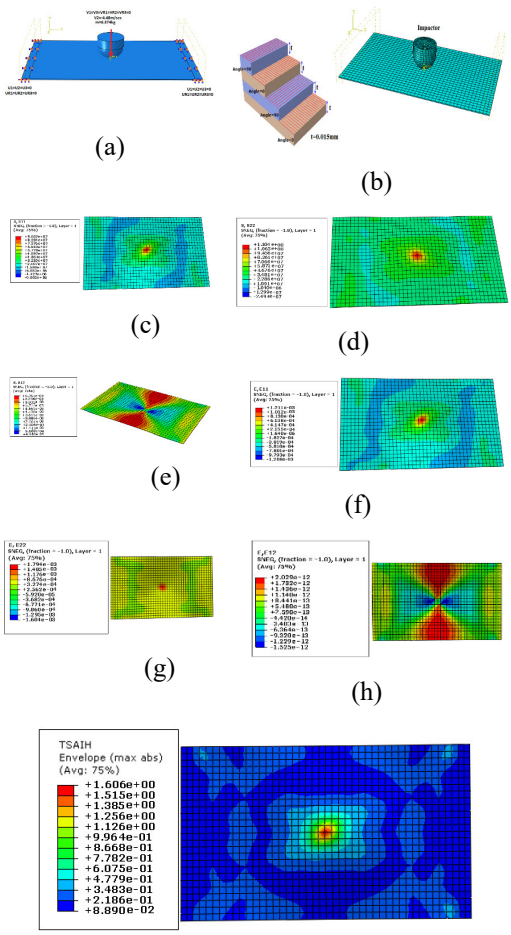

Figure 11: FEM analysis of woven CFRP flat plate with 2 layers and [0°-90°] stacking sequences while subjected to dynamic impact: (a) Model boundaries ; (b) Mesh set up; (c) In plane longitudinal stress (Pa); (d) In plane lateral plane stress (Pa); (e) In plane shear stress (Pa); (f) In plane longitudinal strain; (g) In plane lateral strain; (h) In plane shear strain; (i) Failure index

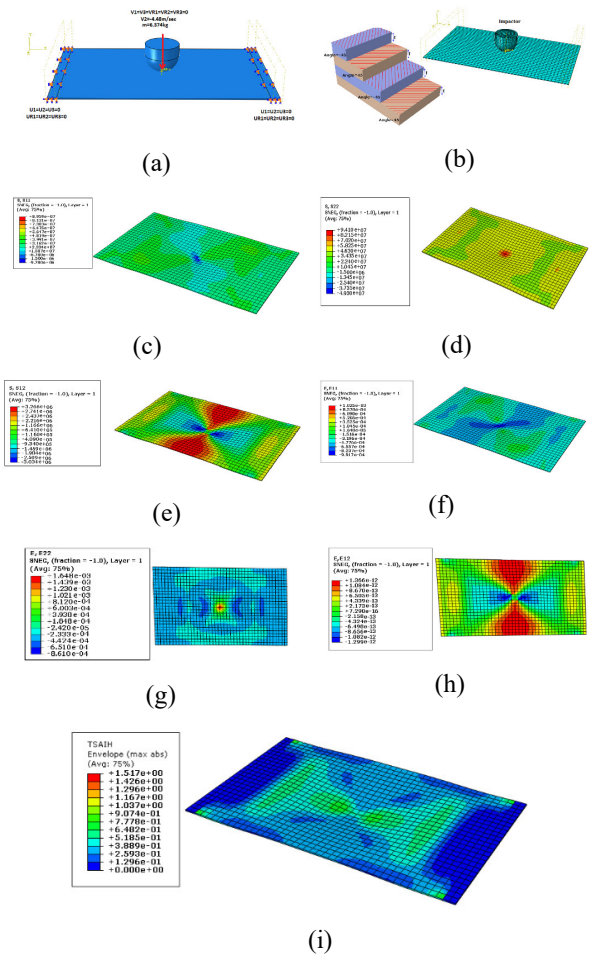

Figure 12: FEM analysis of woven CFRP flat plate with 2 layers and [+45°, -45°] stacking sequences while subjected to dynamic impact: (a) Model boundaries ; (b) Mesh set up; (c) In plane longitudinal stress (Pa); (d) In plane lateral plane stress (Pa); (e) In plane shear stress (Pa); (f) In plane longitudinal strain; (g) In plane lateral strain; (h) In plane shear strain; (i) Failure index

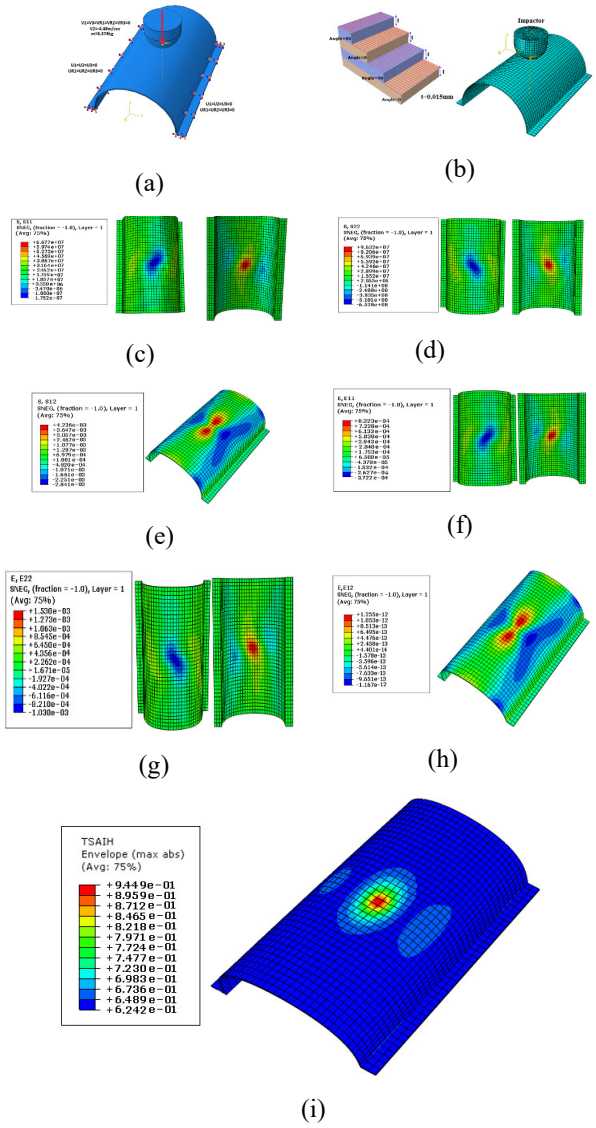

Figure 13: FEM analysis of multi- layered semi-circular corrugated outer patterns made up of woven CFRP corrugated plate with 2 layers and [0°, 90°] stacking sequences while subjected to dynamic impact: (a) Model boundaries ; (b) Mesh set up; (c) In plane longitudinal stress (Pa); (d) In plane lateral plane stress (Pa); (e) In plane shear stress (Pa); (f) In plane longitudinal strain; (g) In plane lateral strain; (h) In plane shear strain; (i) Failure index

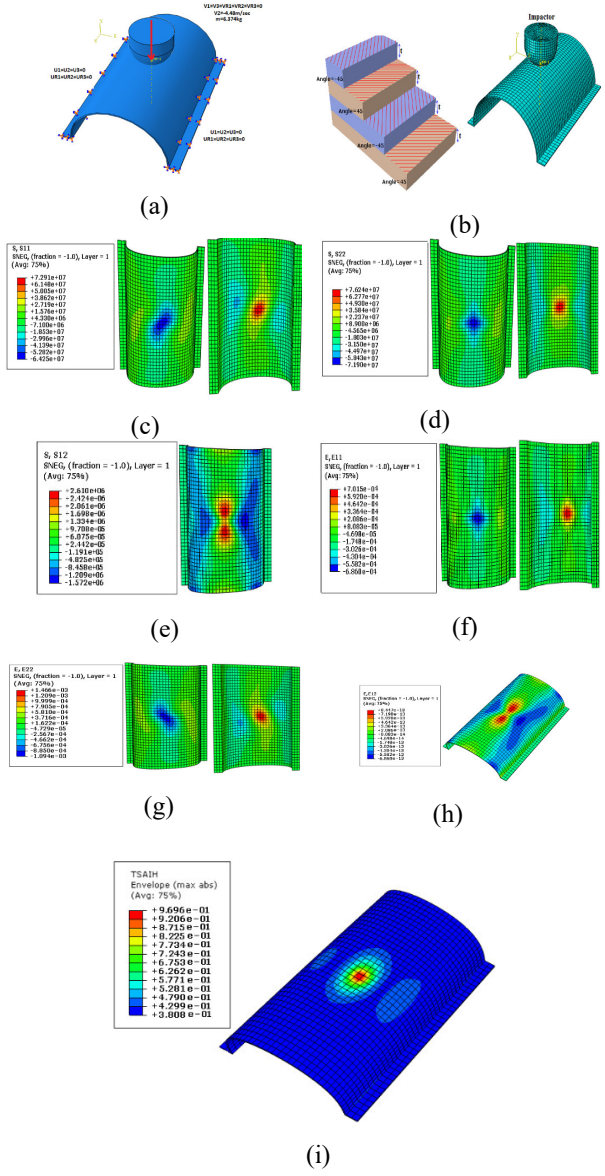

Figure 14: FEM analysis of multi- layered semi-circular corrugated outer patterns made up of woven CFRP corrugated plate with 2 layers and [+45°, -45°] stacking sequences while subjected to dynamic impact: (a) Model boundaries ; (b) Mesh set up; (c) In plane longitudinal stress (Pa); (d) In plane lateral plane stress (Pa); (e) In plane shear stress (Pa); (f) In plane longitudinal strain; (g) In plane lateral strain; (h) In plane shear strain; (i) Failure index

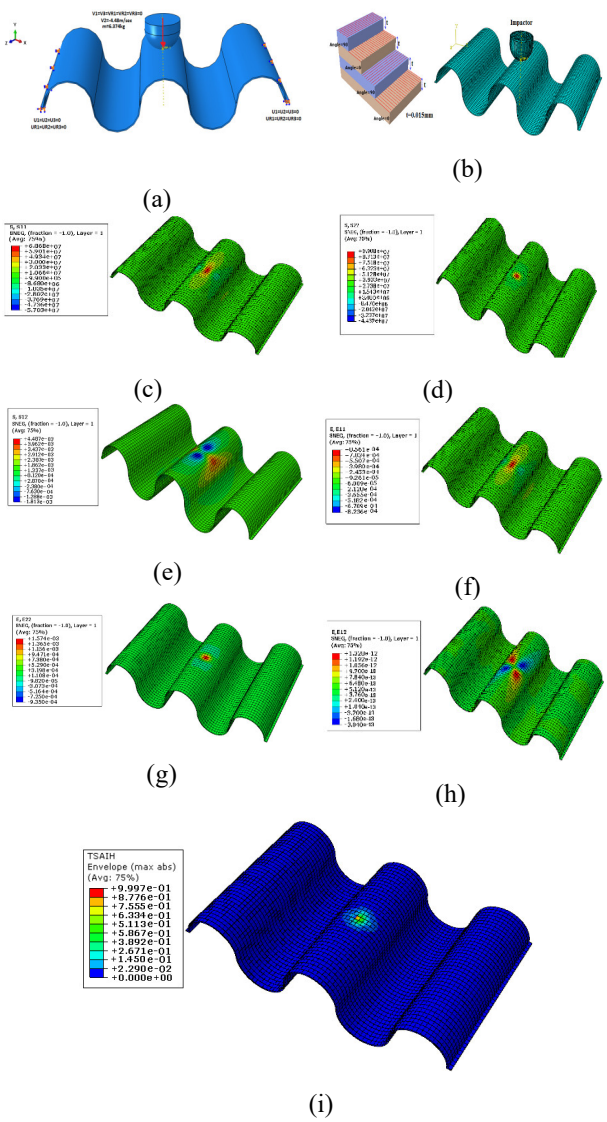

Figure 15: FEM analysis of multi- layered semi-circular corrugated middle patterns made up of woven CFRP corrugated plate with 2 layers and [0°, 90°] stacking sequences while subjected to dynamic impact: (a) Model boundaries ; (b) Mesh set up; (c) In plane longitudinal stress (Pa); (d) In plane lateral plane stress (Pa); (e) In plane shear stress (Pa); (f) In plane longitudinal strain; (g) In plane lateral strain; (h) In plane shear strain; (i) Failure index

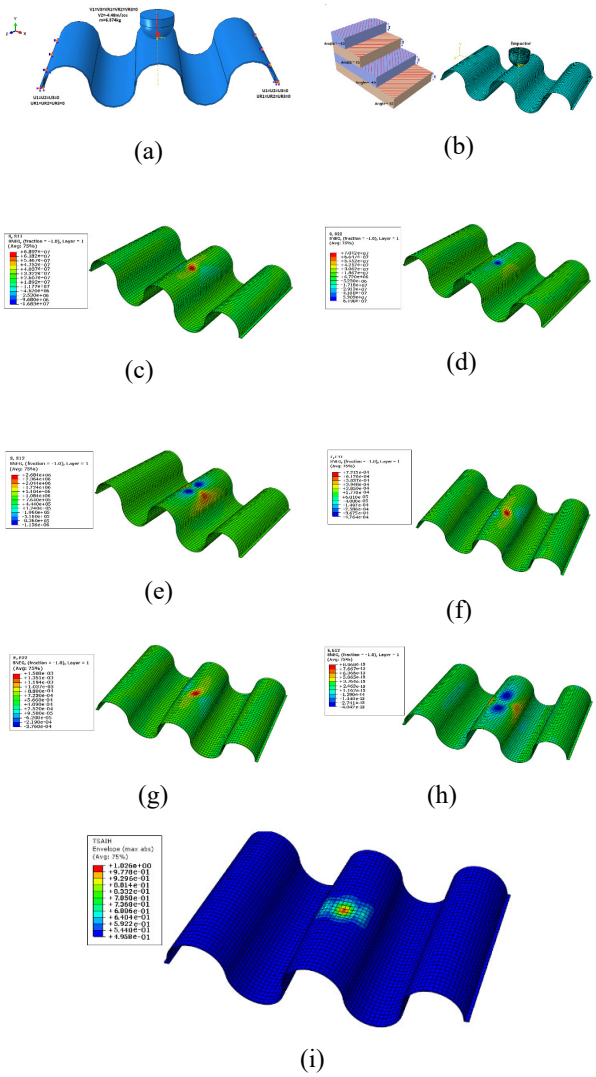

Figure 16: FEM analysis of multi- layered semi-circular corrugated middle patterns made up of woven CFRP corrugated plate with 2 layers and [+45°, -45°] stacking sequences while subjected to dynamic impact: (a) Model boundaries ; (b) Mesh set up; (c) In plane longitudinal stress (Pa); (d) In plane lateral plane stress (Pa); (e) In plane shear stress (Pa); (f) In plane longitudinal strain; (g) In plane lateral strain; (h) In plane shear strain; (i) Failure index

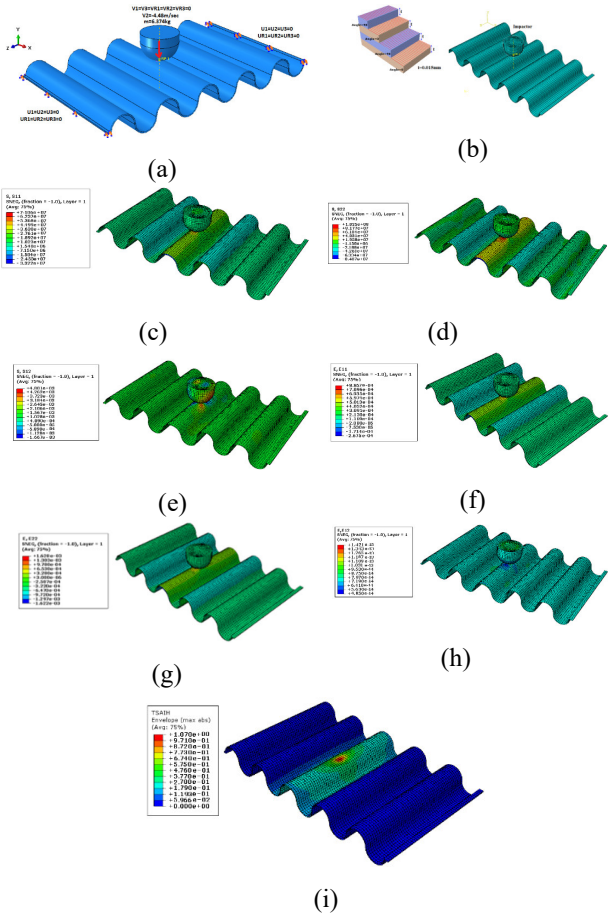

Figure 17: FEM analysis of multi- layered semi-circular corrugated inner patterns made up of woven CFRP corrugated plate with 2 layers and [0°, 90°] stacking sequences while subjected to dynamic impact: (a) Model boundaries ; (b) Mesh set up; (c) In plane longitudinal stress (Pa); (d) In plane lateral plane stress (Pa); (e) In plane shear stress (Pa); (f) In plane longitudinal strain; (g) In plane lateral strain; (h) In plane shear strain; (i) Failure index

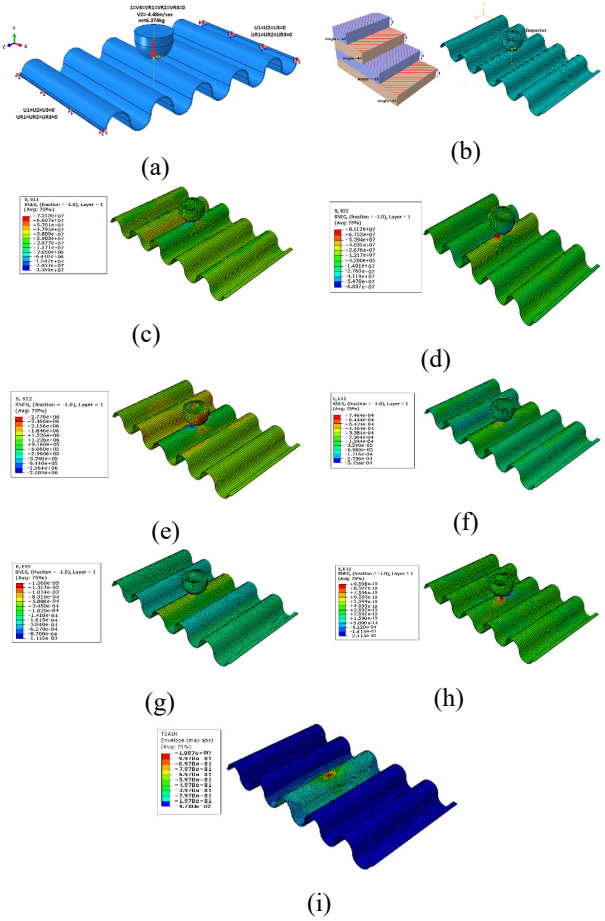

Figure 18: FEM analysis of multi- layered semi-circular corrugated inner patterns made up of woven CFRP corrugated plate with 2 layers and [+45°, -45°] stacking sequences while subjected to dynamic impact: (a) Model boundaries ; (b) Mesh set up; (c) In plane longitudinal stress (Pa); (d) In plane lateral plane stress (Pa); (e) In plane shear stress (Pa); (f) In plane longitudinal strain; (g) In plane lateral strain; (h) In plane shear strain; (i) Failure index

5. Experimental methodology of evaluating Multi- layered semi-circular corrugated woven CFRP plate unit

Stress and failure equations of multi-layered semi-circular corrugated woven CFRP plate unit depends on plane strain. Thus verifying plane strain equation with DIC method admitted the validity of stress and failure equations. Regarding a drop weight set up containing with 16 components as it is depicted in Figure 19, the derived strain equations of multi- layered semi-circular corrugated woven CFRP plate unit can be verified.

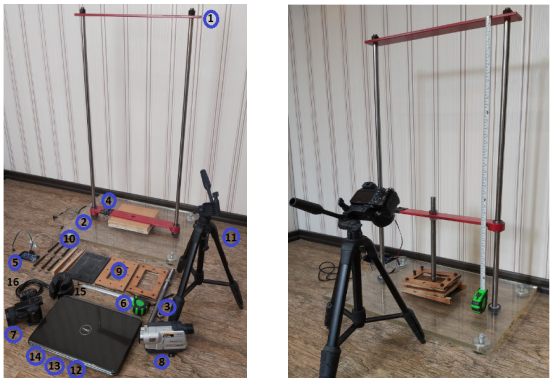

Figure 19: Drop weight set up: (a) Set up parts; (b) Assembly of the drop weight set up

1- Drop weight structure. 2- Guideline bearings. 3-Impactor. 4- MEMS accelerometer sensor. 5- Arduino board. 6- Calibrated ruler. 7-High speed camera with 1200 ($\frac{frame}{sec}$) 8- High speed camera with 1000 ($\frac{frame}{sec}$). 9- Clamp frames. 10- Clamp screws. 11- camera bases. 12- Data recorder. 13- GOM correlate software. 14- Arduino software. 15- flat weights. 16- USB cable.

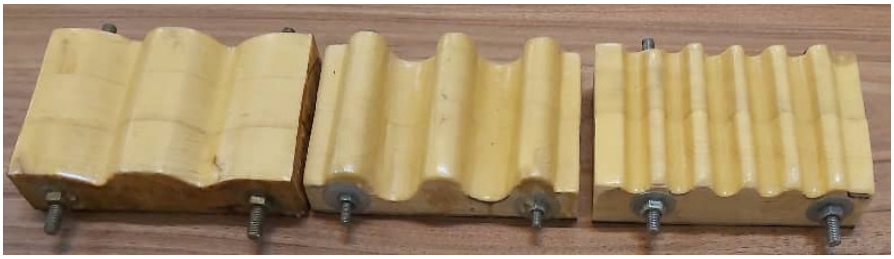

Figure 20: Corrugated wooden molds

Using analytical equations, the Tsai-Hill failure index for two-layered semi-circular corrugated woven CFRP plate unit was found to be the minimum for outer, middle and inner patterns with [0°-90°] and [+45°, -45°] stacking sequences under dynamic impact loading. Thus, corrugated wooden molds in Figure 20 used for manufacturing presented samples in Figure 21.

A scaled-down dynamic impact test is performed for each pattern of multi-layered semi-circular corrugated woven CFRP plate with 2 woven layers including [0°-90°] and [+45°,-45°] stacking sequences based on FMVSS220 standard and DIC method. For the experiments, a spherical nose impactor with a 20 mm nose radius was used, along with the scale down parameters listed in Table 1. The velocity and height of the impactor were detected by MEMS sensor and an electronic Arduino board. A high speed 1000 (frame/sec) camera was used to capture its position along the calibrated ruler. An additional high speed camera, perpendicular to clamped patterns of multi-layered semi-circular corrugated woven CFRP plate, recorded patterns surface displacement with 1200 frames/second. Then, the recorded impact data imported to the GOM DIC computer software to analyse the in plane strain. Figures 22 to 29 illustrate the experimental plane strain results.

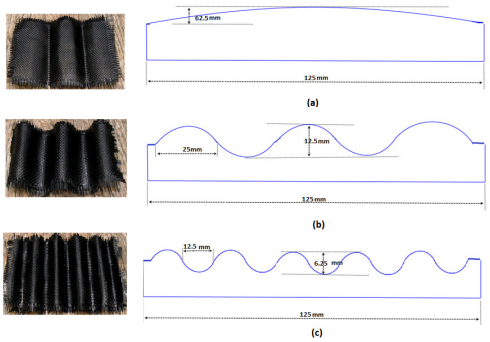

Figure 21: Multi-layered semi-circular corrugated woven CFRP samples: (a) Outer patterns; (b) middle patterns; (c) inner patterns

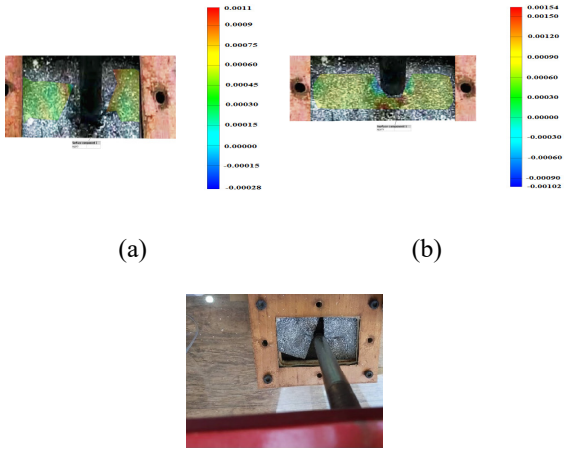

(a) (b)

(c)

Figure 22: DIC plane strain analysis of woven CFRP flat plate with 2 layers and [0°-90°] stacking sequences while subjected to dynamic impact: (a) In plane longitudinal strain; (b) In plane lateral strain; (c) The clamped sample visual situation after impact test

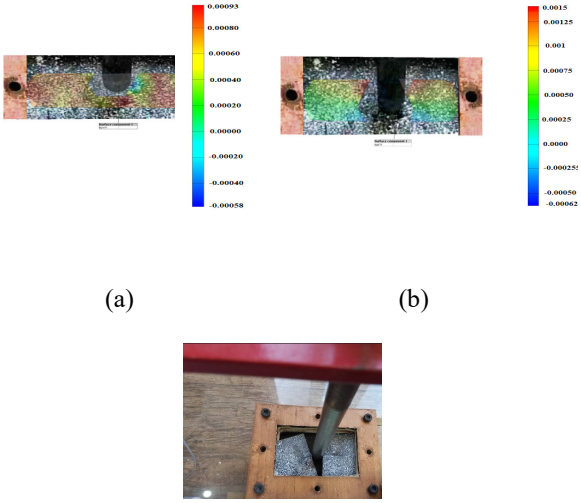

(a) (b)

(c)

Figure 23: DIC plane strain analysis of woven CFRP flat plate with 2 layers and [+45°,-45°] stacking sequences while subjected to dynamic impact: (a) In plane longitudinal strain; (b) In plane lateral strain; (c) The clamped sample visual situation after impact test

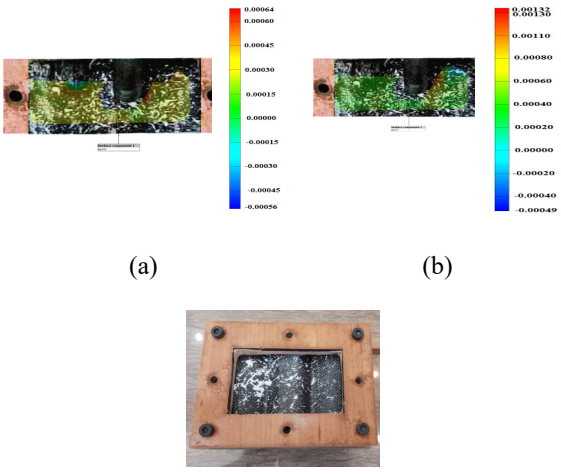

(a) (b)

(c)

Figure 25: DIC plane strain analysis of multi-layered semi-circular corrugated outer patterns made up of woven CFRP corrugated plate with 2 layers and [-45°, -45°] stacking sequences while subjected to dynamic impact: (a) In plane longitudinal strain; (b) In plane lateral strain; (c) The clamped sample visual situation after impact test

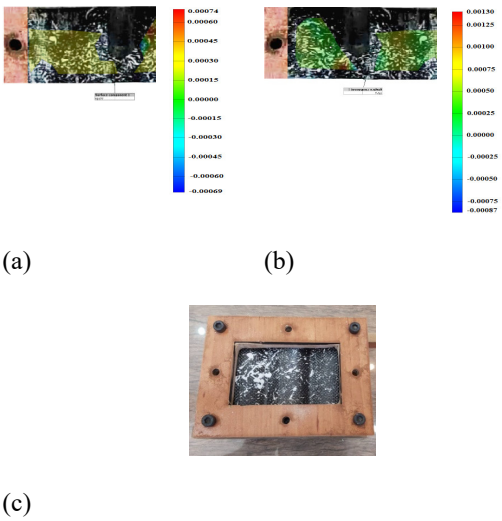

(a) (b)

(c)

Figure 24: DIC plane strain analysis of multi-layered semi-circular corrugated outer patterns made up of woven CFRP corrugated plate with 2 layers and [0°, 90°] stacking sequences while subjected to dynamic impact: (a) In plane longitudinal strain; (b) In plane lateral strain; (c) The clamped sample visual situation after impact test

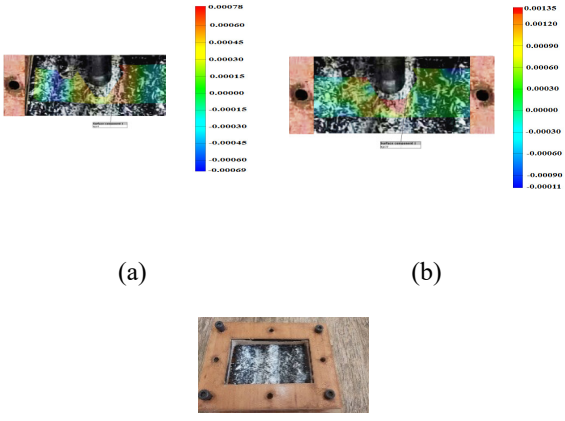

(a) (b)

(c)

Figure 26: DIC plane strain analysis of multi-layered semi-circular corrugated middle patterns made up of woven CFRP corrugated plate with 2 layers and [0°, 90°] stacking sequences while subjected to dynamic impact: (a) In plane longitudinal strain; (b) In plane lateral strain; (c) The clamped sample visual situation after impact test

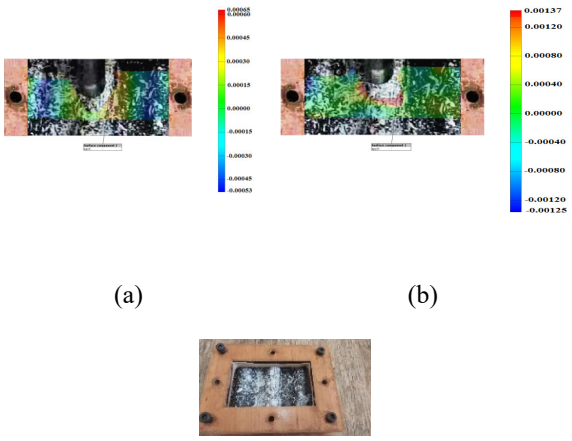

(a) (b)

(c)

Figure 27: DIC plane strain analysis of multi-layered semi-circular corrugated middle patterns made up of woven CFRP corrugated plate with 2 layers and [+45°,-45°] stacking sequences while subjected to dynamic impact: (a) In plane longitudinal strain; (b) In plane lateral strain; (c) The clamped sample visual situation after impact test

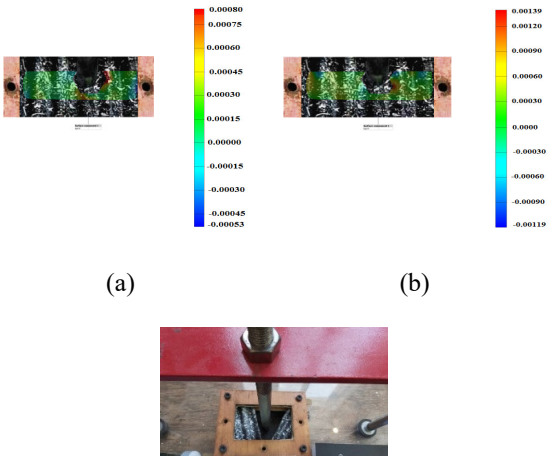

(a) (b)

(c)

Figure 28: DIC plane strain analysis of multi-layered semi-circular corrugated inner patterns made up of woven CFRP corrugated plate with 2 layers and [0°,+90°] stacking sequences while subjected to dynamic impact: (a) In plane longitudinal strain; (b) In plane lateral strain; (c) The clamped sample visual situation after impact test

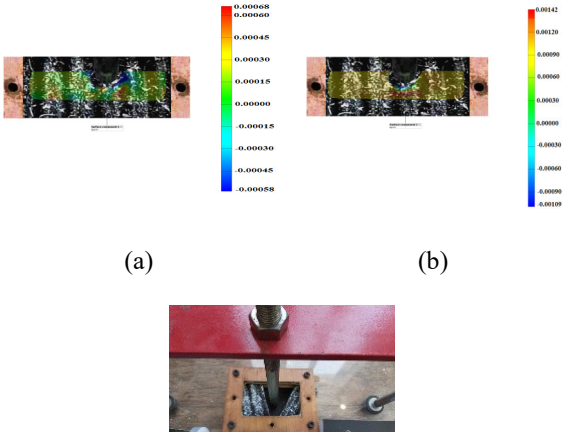

(a) (b)

(c)

Figure 29: DIC plane strain analysis of multi-layered semi-circular corrugated inner patterns made up of woven CFRP corrugated plate with 2 layers and [+45°,-45°] stacking sequences while subjected to dynamic impact: (a) In plane longitudinal strain; (b) In plane lateral strain; (c) The clamped sample visual situation after impact test

6. Discussion

As shown in Figure 8, maximum failure decrease percent for each pattern of multi-layered semi-circular corrugated woven CFRP plate with [0°-90°] and [+45°,-45°] stacking lay ups indicated in Figure 30 in comparison to a flat plate. The outer, middle and inner patterns of the new proposed unit respectively, resulted in 63.43 %, 58.18% and 51.44% of Tsai- Hill index decrease in comparison with the flat plate as both of them have two plies and [0°, 90°] stacking layups. Tsai- Hill damage decrease percent in Figure 30 confirmed [+45°,-45°] stacking sequence as the optimum configuration to decrees failure index for CFRP flat plate, although it is [0°-90°] for semi-circular corrugated woven CFRP plates. Thus 89% damage index reduction for multi- layered semi-circular corrugated unit (Figure 1) was predicted in comparison with flat plate since each pattern contains optimum layer number and stacking sequence (2 layers with [0°, 90°] stacking sequence). Also, layer thickness enhancement caused to decrease the wave effects on each pattern failure because it is proximate to the flat plates.

Based on Figure 30, the outer pattern of the multi-layered semi-circular corrugated woven CFRP plate unit has the lowest Tsai-hill index in comparison with the middle and inner patterns. This means that, wave radius has a much greater effect on failure index decrease than wave number in dynamic impact loading. Thus the maximum possible failure decrease occurred in each pattern. Also, FEM analysis and DIC experiments confirmed these results.

It should be noted that the reliability of suggested analytical equations of traditional and stiffened CFRP plates in predicting their responses under impact depends on their plane strains according to classical laminated theory. Also, the plane shear strain for each corrugated plate is neglected due to its low amount compared to the longitudinal and lateral plane strains. Thus, the difference between the analytical, numerical, and experimental results can be evaluated only with longitudinal and lateral plane strain results. Deviations of strain results conducted from analytical, numerical, and experimental observations are presented in Figures 6 to 29 confirmed that the derived analytical equations could predict the elastic behaviors of CFRP corrugated plates under impact loading.

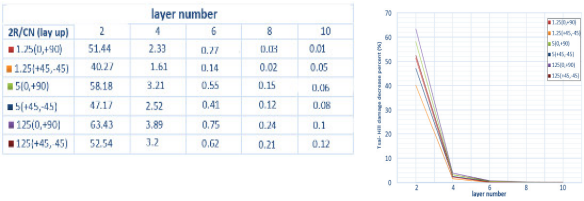

layer number					
2R/CN (lay up)	2	4	6	8	10
1.25(0,+90)	51.44	2.33	0.27	0.03	0.01
1.25(+45,-45)	40.27	1.61	0.14	0.02	0.05
5(0,+90)	58.18	3.21	0.55	0.15	0.06
5(+45,-45)	47.17	2.52	0.41	0.12	0.08
125(0,+90)	63.43	3.89	0.75	0.24	0.1
125(+45, 45)	52.54	3.2	0.62	0.21	0.12

Figure 30: Maximum failure decrease percent for each pattern of multi- layered semi-circular corrugated woven CFRP plate with [0°-90°] and [+45°,-45°] stacking sequence while subjected to dynamic impact loading

7. Conclusion

In this study, we presented a novel configuration of bus roof panel stiffened with multi- layered semi-circular corrugated woven CFRP plates. The strain, stress, and failure equations for multi- layered semi-circular corrugated woven CFRP patterns were derived under a rollover concentrated dynamic impact loading. The derived equations were verified using FEM analysis reports for a loading rollover condition of an 8 ton truck roof panel. Further, a digital image correlation method was used to evaluate the structural failure of the roof panels reinforced with CFRP plates and fabricated using semi-circular corrugations as measured by scaled down FMVSS 220 roll over standards. This study examined the effects of stacking sequence and plies thickness on the mechanical behavior of multi-layered semi-circular corrugated woven CFRP outer, middle and inner patterns subjected to dynamic impact loading. In order to achieve maximum reduction in failure index with each pattern, the best stacking sequence and plies number is [0°-90°] and 2 plies. The outer pattern has the lowest Tsai-hill index in comparison to the middle and inner patterns, meaning that the effects of wave radius on the failure index reduction is greater than the wave number under dynamic impact. Analytical derived equations, FEM software analysis, and experimental drop weight results confirmed 89% positive effects of using multi-layered semi-circular corrugated woven CFRP plates on an 8 ton bus roof panel under rollover dynamic impact loading as compared to flat plates. Therefore, the new proposed multi-layered semi-circular corrugated CFRP plates can be more useful than the typical flat composite plate for a bus roof panel. Further, locating of multi-layered semi-circular corrugated CFRP plates within the structure of bus' roof panel can improve the vehicle's bending stiffness and vibrational behavior, which can be studied as the future work.

Declaration of conflicting interests

The authors confirm that both of them is with Iran University of Science and Technology, and there is not any conflict of interest for this manuscript.

Acknowledgements

The authors received no financial support for the research, authorship, and/or publication of this article.

List of symbols

a	Unit Longitudinal
b	Unit Width
C_n	Semi- circular corrugated woven plate wave numbers
D_{ij}	Matrix of bending stiffness
$D'_{(k).ij}$	Matrix of Curved beam stiffness
E_L	Longitudinal Young's modulus
E_T	Transverse Young's modulus
F	Low- velocity impact loading
G_{LT}	In- plane shear modulus
m, n	counters of Fourier series
$Q^{\theta_k}_{(k)_{,ij}}$	Transformation tensor
R	Semi- circular corrugated woven plate wave radius
S_{12}	In-plane shear strength
$T^{(k)}$	Tsai-Hill failure index for each laminate of composite plate
$T'^{(k)}$	Semi- circular corrugated woven plate Tsai-Hill failure index for each laminate
$w_{(k)}$	Out of plane deflection of each flat laminate
$w'_{(k)}$	Semi- circular corrugated woven plate out of plane deflection
X	Tensile strength (longitudinal)
x	unit reference point
x_0	unit reference point
Y	Tensile strength (transverse)
y	unit reference point
y_0	Impact lateral location from unit reference point
Z_k	Thickness of each ply
$\upsilon_{LT}, \upsilon_{TL}$	Longitudinal and lateral Poisson's ratios
θ_k	Ply angle
ε_x^k	Flat plate longitudinal strain
ε'^k_x	Longitudinal strain of Semi- circular corrugated woven plate
ε_y^k	Transverse strain
ε'^k_y	Corrugated woven plate transverse strain
γ^k_{xy}	Shear strain
γ'^k_{xy}	Semi- circular corrugated woven plate shear strain
σ_x^k, σ_1^k	Flat plate longitudinal stress
$\acute{\sigma}_x^k, \sigma'^k_1$	Corrugated woven plate longitudinal stress
σ_y^k, σ_2^k	Transverse stress
$\acute{\sigma}_y^k, \sigma'^k_2$	Corrugated woven plate transverse stress
τ_{xy}^k, τ^k_{12}	Plate shear stress
$\acute{\tau}_{xy}^k, \tau'^k_{12}$	Corrugated woven plate shear stress

References

[1] Kress, G. and Winkler, M., 2010. Corrugated laminate homogenization model. Composite Structures, 92(3), pp.795-810. https://doi.org/10.1016/j.compstruct.2009.08.027.

[2] Ji, H.S., Song, W. and Ma, Z.J., 2010. Design, test and field application of a GFR corrugated-core sandwich bridge. Engineering Structures, 32(9),pp.2814-2824.https://doi.org/10.1016/j.engstruct.2010.05.001.

[3] Xia, Y., Friswell, M.I. and Flores, E.S., 2012. Equivalent models of corrugated panels. International Journal of Solids and Structures, 49(13),pp.1453-1462. https://doi.org/10.1016/j.ijsolstr.2012.02.023.

[4] Wennberg, D., Stichel, S. and Wennhage, P., 2014. Substitution of corrugated sheets in a

railway vehicle's body structure by a multiple-requirement based selection process. Proceedings of the institution of mechanical engineers, Part F: journal of rail and rapid transit, 228(2), pp.143-157. https://doi.org/10.1177/0954409712467139.

[5] Costas, M., Díaz, J., Romera, L.E., Hernández, S. and Tielas, A., 2013. Static and dynamic axial crushing analysis of car frontal impact hybrid absorbers. International Journal of Impact Engineering, 62, pp.166-181. https://doi.org/10.1016/j.ijimpeng.2013.06.011.

[6] Winkler, M. and Kress, G., 2014. Modeling of corrugated laminates. Composite Structures, 109, pp.86-92. https://doi.org/10.1016/j.compstruct.2013.10.048.

[7] Jiang, Z., Chen, F., Wang, G., Shi, S.Q., Yu, Z. and Cheng, H.T., 2013. Bamboo bundle corrugated laminated composites (BCLC). Part II. Damage analysis under low velocity impact loading. BioResources, 8(1), pp.923-932.

[8] Thurnherr, C., Mirabito, Y., Kress, G. and Ermanni, P., 2016. Highly anisotropic corrugated laminates deflection under uniform pressure. Composite Structures, 154, pp.31-38. https://doi.org/10.1016/j.compstruct.2016.07.017.

[9] Thurnherr, C., Groh, R.M., Ermanni, P. and Weaver, P.M., 2017. Investigation of failure initiation in curved composite laminates using a higher-order beam model. Composite Structures, 168, pp.143-152. https://doi.org/10.1016/j.compstruct.2017.02.010.

[10] Jiang, H., Ren, Y. and Gao, B., 2017. Research on the progressive damage model and trigger geometry of composite waved beam to improve crashworthiness. Thin-Walled Structures, 119, pp.531-543. https://doi.org/10.1016/j.tws.2017.07.004.

[11] Ren, Y., Jiang, H., Ji, W., Zhang, H., Xiang, J. and Yuan, F.G., 2018. Improvement of progressive damage model to predicting crashworthy composite corrugated plate. Applied Composite Materials, 25(1), pp.45-66. https://doi.org/10.1007/s10443-017-9610z.

[12] Ren, Y., Zhang, H. and Xiang, J., 2018. A novel aircraft energy absorption strut system with corrugated composite plate to improve crashworthiness. International Journal of Crashworthiness, 23(1), pp.1-10. https://doi.org/10.1080/13588265.2017.1301082.

[13] Mou, H.L., Su, X., Xie, J. and Feng, Z.Y., 2018. Parametric analysis of composite sinusoidal specimens under quasi-static crushing. https://doi.org/10.1017/aer.2018.64.

[14] Mehdikhani, M., Gorbatikh, L., Verpoest, I. and Lomov, S.V., 2019. Voids in fiber-reinforced polymer composites: A review on their formation, characteristics, and effects on mechanical performance. Journal of Composite Materials, 53(12), pp.1579-1669. https://doi.org/10.1177/0021998318772152.

[15] Rong, Y., Liu, J., Luo, W. and He, W., 2018. Effects of geometric configurations of corrugated cores on the local impact and planar compression of sandwich panels. Composites Part B: Engineering 152, pp.324-335.https://doi.org/10.1016/j.compositesb.2018.08.130.

[16] Zhang, Z., Lei, H., Xu, M., Hua, J., Li, C. and Fang, D., 2019. Out-of-plane compressive performance and energy absorption of multi-layer graded sinusoidalcorrugated sandwich panels. Materials & Design, 178, p.107858.https://doi.org/ 10.1016/j.matdes.2019.107858.

[17] Mohammadabadi, M., Yadama, V. and Smith, L., 2019. An analytical model for wood composite sandwich beams with a biaxial corrugated core under bending. Composite Structures,228,p.111316.https://doi.org/10.1016/j.compstruct.2019.111316.

[18] Affolter, C., Barbezat, M., Piskoty, G., Steger, R. and Terrasi, G., 2019. Testing strategies and failure modes of dimpled laminate

plates. Engineering Failure Analysis, 101, pp.283-297. https://doi.org/10.1016/j.engfailanal.2019.03.011.

[19] Farrokhabadi, A., Taghizadeh, S.A., Madadi, H., Norouzi, H. and Ataei, A., 2020. Experimental and numerical analysis of novel multi- layered sandwich panels under three point bending load. Composite Structures, 250, p.112631.https://doi.org/10.1016/j.compstruct.2020.112631.

[20] Wang, Y. and Chang, F.K., 2022. Numerical and experimental evaluation of mechanical performance of the multifunctional energy storage composites. Journal of Composite Materials, 56(2), pp.199-212.https://doi.org/10.1177/00219983211049504.

[21] Azadian, M., Hasani, H. and Shokrieh, M.M., 2018. Flexural behavior of composites reinforced with innovative 3D integrated weft-knitted spacer fabrics. Journal of Industrial Textiles, 48(1), pp.58-76. https://doi.org/10.1177/1528083717721923.

[22] Djama, K., Michel, L., Ferrier, E. and Gabor, A., 2020. Numerical modelling of a truss core sandwich panel: Influence of the connectors' geometry and mechanical parameters on the mechanical response. Composite Structures, 245, p.112335. https://doi.org/10.1016/j.compstruct.2020.112335.

[23] Bacciocchi, M. and Tarantino, A.M., 2020. Critical buckling load of honeycomb sandwich panels reinforced by three-phase orthotropic skins enhanced by carbon nanotubes. Composite Structures, 237, p.111904. https://doi.org/10.1016/j.compstruct.2020.111904.

[24] Eyvazian, A., Taghizadeh, S.A., Hamouda, A.M., Tarlochan, F., Moeinifard, M. and Gobbi, M., 2019. Buckling and crushing behavior of foam-core hybrid composite sandwich columns under quasi-static edgewise compression. Journal of Sandwich Structures & Materials,p.1099636219894665.https://doi.org/10.1177/1099636219894665.

[25] Eyvazian, A., Moeinifard, M., Musharavati, F., Taghizadeh, S.A., Mahdi, E., Hamouda, A.M. and Tran, T.N., 2021. Mechanical behavior of resin pin-reinforced composite sandwich panels under quasi-static indentation and three-point bending loading conditions. Journal of Sandwich Structures & Materials, 23(6), pp.2127-2145. https://doi.org/10.1177/1099636220909752.

[26] Liang, C.C. and Nam, L.G., 2010. Comparative analysis of bus rollover protection under existing standards. WIT Trans. Built Environ, 113, pp.41-53.

[27] Fay R J, Wittrock EP. Scale- Model Test of an Energy-absorbing barrier. Highway research record. 1971;343:75-82.

[28]Christos, K., 2010. Design and analysis of composite structures: with application toaerospace structures. Willey, Chichester, UK, pp.300-306.

[29] Hyer, Michael W., and Scott R. White., 2009. Stress analysis of fiber-reinforced composite materials. DEStech Publications.

[30] Daniel, I.M. and Ishai, O., 2006. Engineering mechanics of composite materials, 2nd edition, Oxford University Press.

[31] Standard, A.S.T.M., 2008. Standard test method for tensile proprieties of polymer matrix composite materials. ASTM D3039/DM, 3039(2008).